

Modeling and simulation of tumor-influenced high resolution real-time physics-based breast models for model-guided robotic interventions

John Neylon, Katelyn Hasse, Ke Sheng and Anand P Santhanam
Department of Radiation Oncology, University of California, Los Angeles, CA, USA

ABSTRACT

Breast radiation therapy is typically delivered to the patient in either supine or prone position. Each of these positioning systems has its limitations in terms of tumor localization, dose to the surrounding normal structures, and patient comfort. We envision developing a pneumatically controlled breast immobilization device that will enable the benefits of both supine and prone positioning. In this paper, we present a physics-based breast deformable model that aids in both the design of the breast immobilization device as well as a control module for the device during every day positioning. The model geometry is generated from a subject's CT scan acquired during the treatment planning stage. A GPU based deformable model is then generated for the breast. A mass-spring-damper approach is then employed for the deformable model, with the spring modeled to represent a hyperelastic tissue behavior. Each voxel of the CT scan is then associated with a mass element, which gives the model its high resolution nature. The subject specific elasticity is then estimated from a CT scan in prone position. Our results show that the model can deform at >60 deformations per second, which satisfies the real-time requirement for robotic positioning. The model interacts with a computer designed immobilization device to position the breast and tumor anatomy in a reproducible location. The design of the immobilization device was also systematically varied based on the breast geometry, tumor location, elasticity distribution and the reproducibility of the desired tumor location.

Keywords: biomechanical modeling, breast immobilization, radiotherapy

1. INTRODUCTION

Breast cancer patients typically receive a breast conserving procedure of surgically resecting the gross tumor with margin (lumpectomy), or a more extensive area of tumor surrounding breast tissue plus chest muscle lining (partial mastectomy). In these breast-conserving procedures, to sterilize possible stray cancer cells, post-surgical radiotherapy on the whole breast or partial breast (the surgical bed and involved lymph nodes) is typically administered[1]. While this treatment approach has achieved tremendous success in reducing tumor recurrence, there is substantial risk of treatment-related toxicity in the healthy tissues surrounding the breast anatomy. The soft and deforming breast anatomy results in an unstable shape and position[2]. For partial breast treatment to the surgical bed, the uncertainty increases the required geometrical margins during radiotherapy treatment planning and the subsequent normal breast tissue gets exposed to higher radiation doses[3].

1.1. Supine positioning

When patients are in the typical supine orientation (Figure 1(a)), the breast is weighed down by the gravity and spreads to have a large contact area with the chest wall. A considerable amount of underlying normal anatomies including heart, lung and skin in the infra-mammary folds are thus exposed to a high radiation dose leading to significant radiation side-effects (dermatitis, fibrosis, fat necrosis and lung radiation pneumonitis and a significant risk for cardiac problems). The breast shape in the supine orientation, by itself, is problematic for radiation planning as radiation hot spots (tissues receiving doses greater than the prescription dose) are often unavoidable and further worsens the side effects. Reducing treatment related toxicity for both the breast anatomy as well as its surrounding thoracic organs is critical to improve radiotherapy treatment outcomes[4, 5].

1.2. Prone positioning

Methods that alleviate treatment related toxicity have focused on modulating patient orientation. Specifically, prone patient orientation on a breast couch with a “drop-in cut-out” allows gravity to move the breast away from the patient (Figure 1(b)). This set up significantly reduces the lung and chest wall doses and result in less severe hot spots inside the breast[1]. However, prone set-up results in a descending heart position that increases cardiac doses in some patients. Setting up the patient in a prone orientation is also more difficult, leading to a poorer reproducibility as compared to a supine orientation. Many patients cannot tolerate prone position for the typical treatment duration. Furthermore, lymph node coverage is more difficult in the prone orientation.

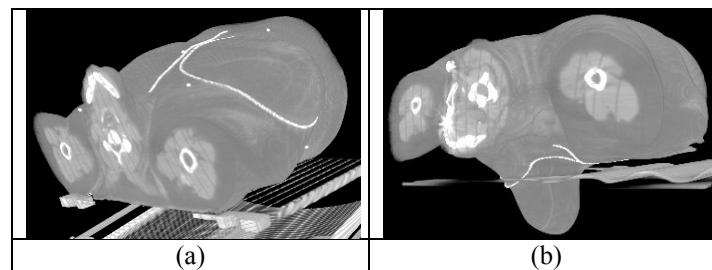


Figure 1. Volume renderings of supine (a) and prone (b) CTs of the same patient demonstrating significant differences in breast anatomy due to posture and the desired separation of the breast from the chest wall achieved in prone orientation.

1.3. Breast immobilization

Achieving ideal breast geometry (similar to prone orientation) for treating the tumor in a supine orientation using an effective robotic assistance forms the focus of this proposal. Such a robotic assistance must incorporate the benefits of both the supine orientation and provide active immobilization system engineering with materials that will not increase the skin irradiation. A soft robotics based design addresses the aforementioned problems by using a thin and light material and providing a soft robot-breast interface so that the patient can comfortably tolerate the manipulation. We envision a soft robotics based system for developing a breast immobilization device for precise breast tumor targeting while minimizing dose to the cardiac region. Specifically, the robotic system consists of multiple dough-nut shaped pneumatically inflatable chambers that when placed around the breast anatomy can be inflated to immobilize the breast during radiotherapy. We envision a high-resolution physics-based breast model as a control module for the proposed robotic system, which forms the focus of this paper. A key knowledge gap exists in the application of soft robotics for positioning such delicate and deformable anatomies. Addressing this knowledge gap forms the technical focus of this paper.

1.4. Biomechanical modeling and elasticity

Sophisticated biomechanical models have been developed for individual anatomical sites, including the head and neck[6], the hand[7, 8], lungs[9], and the leg[10]. Physics-based methods, such as finite element and mass-spring, allow for a broad array of simulations. Models are typically generalized and limited in focus to specific sites and types of motion or interaction due to computational complexity. The time for highly complicated simulations can take minutes to hours on a CPU. A framework was developed to generate patient-specific, GPU-based biomechanical models using a mass-spring-damper system where each mass represents a voxel from a patient CT scan for the purpose of validating clinical non-rigid registrations by creating ground truth deformations[11]. The linear elastic physics of the model ran entirely on GPU in a multi-level algorithm. With this methodology, interactive speeds (>30 fps) were achieved on a single GPU for approximately 1.5 million mass elements with over 25 million connections. The soft tissue response was accurate with an R^2 value of > 0.98 when compared to ground-truth global and local force deformation analysis. For a clinically relevant range of posture and physiological changes, the model deformations stabilized with an uncertainty of less than 0.01 mm.

Historically, soft tissues have been modeled using linear elastic properties for simplicity and speed, as was the initial development of the model described above. This is a reasonable approximation for small deformations, such as the limited day to day variations caused by weight loss, tumor regression, or small posture changes. However, the differences in the breast anatomy between the supine and prone positioning results in much larger deformations. Most biological tissues exhibit a hyper-elastic response [12, 13], meaning they are virtually incompressible but able

to undergo large elastic deformations. Maintaining an interactive framerate for a hyper-elastic material model implementation is much more difficult than a linear Hookean model[14] due to the complex system of non-linear equations that must be solved for each frame.

2. METHODS

2.1. Forward deformation computation

The model consisted of a GPU based biomechanical soft-tissue model with each voxel being associated with a mass (referred to as mass elements) and connected by mesh lattice. The model elements are isotropically spaced and interconnected by a set of visco-elastic springs to form a high-resolution biomechanical breast model. The elastic properties of the connections were assigned according to values reported in literature from previous elastography studies[15-18]. The model was initially developed using linear elasticity, described by the stress/strain relationship of Hooke's law[19], as in equation 2 where σ is the stress tensor, ϵ is the strain tensor, and S is stiffness matrix defined by Lamé's parameters,

$$\sigma_{ij} = S_{ijkl}\epsilon_{kl} . \quad (1)$$

Hyper-elasticity was formulated by deriving a strain-energy function from the deformation gradient tensor, \mathbf{F} ,

$$F_{ij} = \frac{\partial x_i}{\partial X_j} . \quad (2)$$

Where \mathbf{X} represents the reference state of a component, and \mathbf{x} represents the deformed state. This can be rewritten as the product of a rotation matrix \mathbf{R} and a rotationally independent deformation tensor \mathbf{U} or \mathbf{V} ,

$$\mathbf{F} = \mathbf{R} \cdot \mathbf{U} = \mathbf{V} \cdot \mathbf{R} . \quad (3)$$

The stretch tensors and deformation gradient tensor can easily be calculated from the known state of the model by analyzing the local deformation around each element using the nearest neighbor connections. The right Cauchy-Green deformation tensor can then be directly derived,

$$C_{ij} = F_{ki}F_{kj} . \quad (4)$$

The principal stretches, λ_i , can be found by solving for the real roots polynomial relating the stretch invariants, I_i^C , of the Cauchy-Green deformation tensor. The stretch invariants are defined as follows,

$$I_1^C = C_{ii} = tr(C) , \quad (5a)$$

$$I_2^C = \frac{1}{2}(C_{ii}C_{jj} + C_{ij}C_{ji}) , \quad (5b)$$

$$I_3^C = \epsilon_{ijk}C_{i1}C_{i2}C_{i3} = \det(C) , \quad (5c)$$

$$\lambda^3 - \lambda^2 I_1^C + \lambda I_2^C - I_3^C = 0 . \quad (5d)$$

Hyper-elasticity was implemented using a generalized Ogden material model, which defines the strain energy, W , in terms of the principal stretches, λ_i , and the shear modulus, μ [20]. The principal stretches can be found by solving for the eigenvectors of the deformation tensor (\mathbf{U} or \mathbf{V}). The Ogden model allows experimentation with a variety of strain-energy functions by adjusting the parameters N and α , such as Neo-Hookean ($N = 1, \alpha = 2$)[21] and Mooney-Rivlin ($N = 2, \alpha_1 = 2, \alpha_2 = -2$)[22, 23], according to assumptions such as incompressibility, to simplify the strain energy function,

$$W = \sum_{p=1}^N \frac{\mu_p}{\alpha_p} (\lambda_1^{\alpha_p} + \lambda_2^{\alpha_p} + \lambda_3^{\alpha_p} - 3) , \quad (6)$$

$$2\mu = \sum_{p=1}^N \mu_p \alpha_p . \quad (7)$$

After applying a polar decomposition to the strain energy function, it can be rewritten as a combination of a deviatoric and hydrostatic term, f_p , separating out the volumetric work of the deformed state,

$$W = \tilde{W} + f_p = \sum_{p=1}^N \frac{\mu_p}{\alpha_p} (\tilde{\lambda}_1^{\alpha_p} + \tilde{\lambda}_2^{\alpha_p} + \tilde{\lambda}_3^{\alpha_p} - 3) + f_p, \quad (8)$$

$$\tilde{\lambda}_i = \lambda_i (I_3^C)^{-1/6}. \quad (9)$$

The principal Cauchy stresses, σ_i , can be found from the 2nd Piola-Kirchoff stress tensor, τ , which is derived from the partial derivative of the strain energy function with respect to the principal stretches[24, 25]. The hydrostatic pressure term, f_p , disappears under the assumption of incompressibility typically applied for biological tissues,

$$\sigma_i = \lambda_i \tau_i = 2\lambda_i \frac{\partial \tilde{W}}{\partial \lambda_i} = \sum_{p=1}^N \mu_p \lambda_i^{\alpha_p}. \quad (10)$$

From the principal Cauchy stress at each element, the internal force vectors, \tilde{f}_a , can be computed[26], and the new positions, \tilde{x}_a^{n+1} , and velocities, \tilde{v}_a^{n+1} , of the mass elements updated from the values ($\tilde{x}_a^n, \tilde{v}_a^n$) at the previous iteration n , using Implicit (Backward) Euler integration.

$$\tilde{v}_a^n = \tilde{v}_a^n + \left(\frac{\tilde{f}_a}{m_a} + \tilde{g} \right) \delta, \quad (11.a)$$

$$\tilde{x}_a^n = \tilde{x}_a^n + \tilde{v}_a^n \delta, \quad (11.b)$$

where δ was the time step between iterations, m_a was the mass of mass element a , and \tilde{g} was acceleration due to gravity. To improve robustness and stability, at a compromise with performance, the trapezium rule was applied to the implicit integration scheme according to Heun's method[27, 28]. Thus, the velocity and position were calculated using the above methodology but applying a time update of $\delta/2$. The intermediate internal force vectors were recalculated according to this intermediate deformation state to allow compensation. Finally, the model was updated by equally weighting the two components.

2.2. Surface triangulation

Particle-particle interactions can be unstable for prolonged contact forces such as the surface interactions between an immobilization device and breast model. Therefore, a triangulated surface was constructed to encase the breast model. Surface triangulation remains an active area of research, with many algorithms to convert point cloud information to polygonal faces. These include marching cubes[29], marching triangles[30], the ball-pivoting algorithm[31], and Poisson reconstruction[32]. Concepts were adapted and modified from these surface reconstruction algorithms to utilize the established connections from our meshing algorithm to facilitate surface triangulation.

The meshing algorithm employed during instantiation of the model produces isotropic connections about each element. Surface elements were identified by summing the normalized directional vectors of all connections belonging to each element, and dividing by the maximum number of possible connections. For any element with less than the maximum number of connections, the magnitude of this summed directionality vector would be greater than zero. A threshold can adjust the sensitivity of the surface element identification to the number of missing connections.

Once all surface elements were identified, a list of possible edges were created by finding all existing connections between surface elements. These edges were then iterated through and concatenated to find triplets of edges with matching vertices. A series of conditions were imposed to optimize the generation of triangles, and account for the irregular geometry of patient anatomy which may not be entirely convex. This included prioritizing edges that already belonged to a single triangle face, disallowing the addition of new edges to the open edge list, tests based on the principles of the ball-pivoting algorithm[31] and vector algebra test to prevent overlapping of triangle faces. The ball-pivoting algorithm test finds the sphere that would sit on each vertex of the proposed triangle face, with the

sphere's center in the direction of the triangle normal. By testing that no other vertices reside within this sphere, it ensures that faces are truly on the surface and not cutting corners. However, this has limitations when applied to non-convex objects, which are common when considering anatomical structures. Therefore, an additional loop wrapped the triangle search algorithm, toggling different criteria to fill gaps when the algorithm stalls.

2.3. Biomechanical breast model as a control mechanism

A mechanism was implemented to anchor a selected portion of the breast model to a simulated 'chest wall'. A wireframe sphere was rendered in the deformation space, giving user control to the radius and center of the sphere, such that any elements of the breast model that fell within the volume of the sphere were anchored and immovable. This effectively replaced the patient torso, simplifying the simulation and providing the user with control of the anchoring of the breast model, as well as a mechanism for introducing slight posture changes such as roll, pitch, and yaw by simply rotating the wireframe sphere.

To simulate deformations, we applied the gravity as a uniform force on each of the soft breast tissue element in a series of slightly different orientations to approximate day-to-day posture changes that may be seen clinically. In addition, volume conserving anatomical deformations forms a critical role in facilitating a precise biomechanical deformation. Incorporating volume conservation, from a biomechanical perspective, refers to the fact that the breast tissue undergoes minimal volume change when the subject's posture changes from supine to prone. From the triangulated surface of the object, the volume can be estimated by summing over the surface triangles[33]. A constraint force based on the Jacobian distribution can then be incorporated to preserve the volume as the model integrates positions.

3. RESULTS

3.1. Forward deformation and elasticity

Figure 2(a) displays a representative model of the breast, where the static chest wall anchor is black and the deformable breast tissue is blue. Figures 2(b) and 2(c) show the deformation due to gravity for two orientations. This simplistic representation was able to reasonably reproduce observed behavior of breast anatomy due to gravity after optimizing the elastic values throughout the volume. In validation of the elasticity estimation methodology, convergence occurred when the estimated displacement was within 1 mm of the ground-truth displacement for each voxel. Our analysis shows that an accuracy of 98% was achieved in reconstructing ground-truth elasticity distributions.

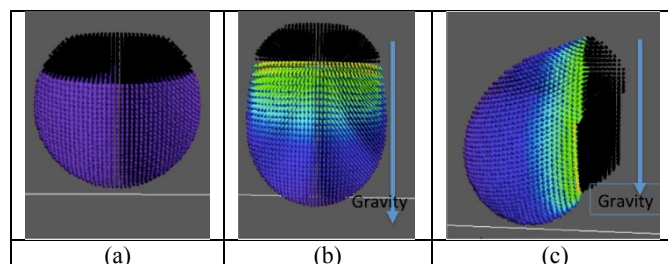


Figure 2. A 3D deformable model of the breast is shown (a). The breast anatomy is represented in blue while the rib-cage wall is shown in black. The deformation of the model under gravity is shown for the two orientations in (b) and (c), respectively, with the color map representing the local deformation.

3.2. Surface triangulation

Figure 3 shows the progression of the model instantiation in four stages. Figure 3(a) displays the representative breast volume after the individual elements had been localized in the deformation space. Figure 3(b) displays the results of the meshing algorithm. Here each element is shown as a white point, while the connections are color

coded to correspond to the spherical element representations in figure 3(a). Figure 3(c) shows the result of the surface element identification. All elements are shown as black points, but the surface elements have their normal vectors emanating from them and color coded to correspond with the colors of the spherical elements of figure 3(a). Finally, figure 3(d) shows the final triangulated surface for the volume. Elements are shown again as black points, while each triangle face was rendered with vertices color coded to match figure 3(a). Additionally, the normal for each triangle face are rendered as white lines, originating from the center of the circle inscribed within its parent triangle.

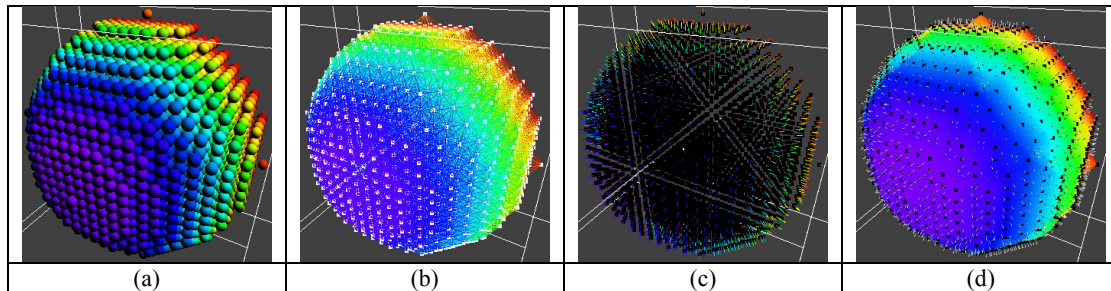


Figure 3. An example of the progression from a collection of elements (a), to the fully connected mesh (b), to the identified surface elements and their associated normals (c), and finally the watertight triangulated surface (d).

3.3. Initializing patient data and simulating the chest wall anchor

Figure 4 shows the creating of a patient specific breast model. Figure 4(a) shows the full patient anatomy loaded from a supine CT. The anatomy was divided between the right breast, the skeletal anatomy, and general soft tissues. The full anatomy model consisted of more than 750,000 elements. Each structure has a bounding box that indicates possible interactions. Figure 4(b) removes the general soft tissues, displaying only the breast and the skeletal anatomy. Figure 4(c) additionally removes the skeletal anatomy, leaving only the breast tissue model. The breast alone contributed just over 36,000 elements with over 400,000 connections between them. Of the 36,000 elements in the breast model, 9600 were identified as surface elements with 59,000 possible edges between them, resulting in over 13,500 surface triangles. In figure 4(d), the torso was replaced with a wireframe sphere. All elements within the radius of the wireframe sphere are considered anchored to the sphere, and are shown as black in the image. In figure 4(e), a simple immobilization device consisting of three pneumatic tori, where both inner and outer radii can be adjusted to lift and separate the breast away from the simulated chest wall. This immobilization model is discussed in more detail in the following section. The model described in figure 4 performed at approximately 68 frames per second using a hyper-elastic material model and improved Euler integration on a single GPU. For comparison, a linear elastic material model with implicit Euler integration ran at approximately 78 frames per second for the same breast model.

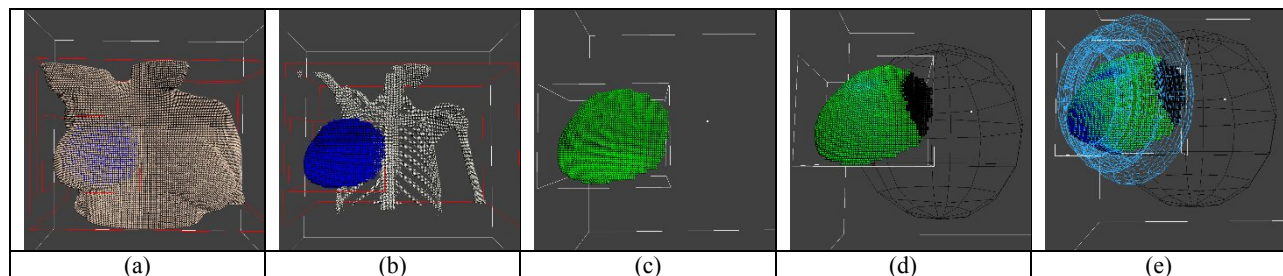


Figure 4. The instantiation and extraction of a patient specific breast model is displayed. (a) show the full patient anatomy from a supine CT. (b) removes general soft tissues, displaying the skeletal anatomy and breast model. (c) displays just the breast model. (d) introduces a wireframe sphere to represent the patient torso and provide a chest wall anchor for the breast model. (e) shows how a possible immobilization device could be rendered and applied to the breast model.

The replacement of the actual patient torso with a wireframe sphere simplifies the simulation and facilitates the testing for a spectrum of subtle posture changes, such as those that may be seen clinically from day to day. Changes to the roll, pitch, and yaw of the anatomy can be simulated by simple rotations about the center of the sphere. Figure

5 illustrates this effect, displaying the differences in breast anatomy due to gravity from these small posture changes. This provides a platform for testing the immobilization device's ability to provide consistent reproducible geometry, despite the highly variable nature of the anatomy.

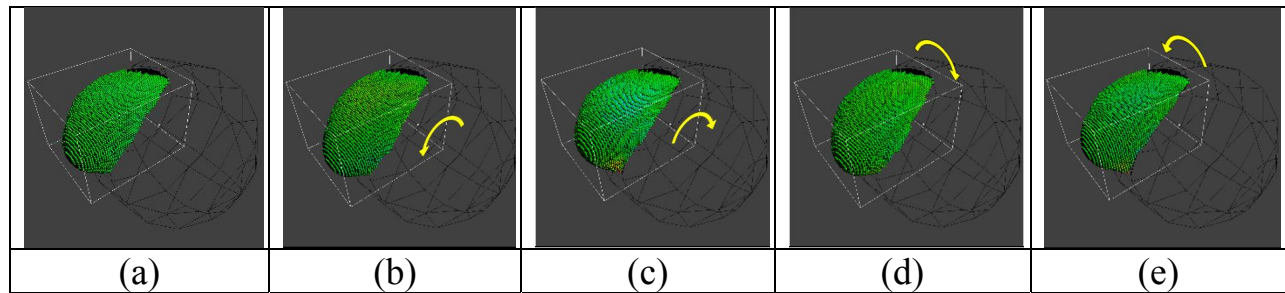


Figure 5. Illustrating subtle posture changes by introducing roll, pitch, and yaw with the wireframe sphere chest wall anchor. (a) shows the initial breast posture from the supine CT data, with the wireframe sphere anchoring the chest wall. (b) shows an ipsilateral roll, and (c) shows a contralateral roll. (d) and (e) show pitches in the caudal and cranial directions, respectively.

3.4. Manipulating breast anatomy with a simulated immobilization device

Figure 6(a) shows the initial breast and upper thoracic structure and its non-rigid interaction between a pneumatic multi-compartment rigid model is shown in figures 6(b) and 6(c). The 3D deformable anatomy is color-coded to represent the stress and strain on each finite element (green-blue representing compression and green-red representing extension). Such local variations in the deformable structure's stress points to the need for such a deformable breast model in order to minimize any patient discomfort during positioning. The GPU implementation was able to maintain an interactive frame rate (>30 fps) when manipulating the rigid immobilization device, for a model with over 1 million total elements and approximately 65,000 within breast anatomy region of interest.

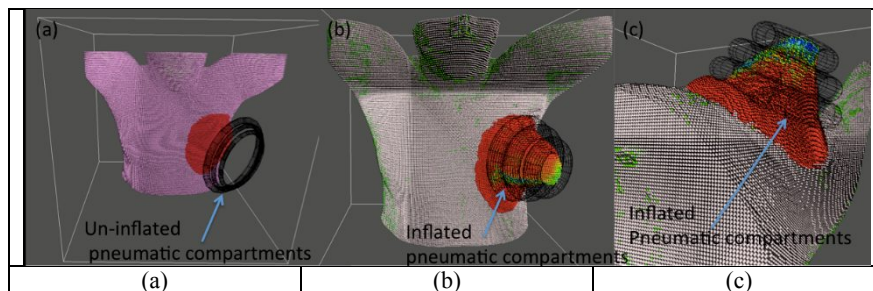


Figure 6. Biomechanical simulation of pneumatic soft-robotics based breast positioning. (a) shows the breast anatomy and the robotic system before being pneumatically inflated. (b) and (c) shows a biomechanical simulation of the pneumatic air inflation and the corresponding breast deformation.

4. DISCUSSION AND CONCLUSION

The key breakthrough presented in this work is the capability for instantiation and interactive manipulation of patient-specific hyper-elastic breast models, which provides a platform to design and test novel breast immobilization devices with realistic and accurate breast tissue response, and the ability to perform systematic evaluation of the device's reliability and reproducibility for immobilizing the breast and localizing the tumor target for external beam radiotherapy on actual clinical patient data. There remains ample room for further development of the model. Two avenues for future work are presented below.

4.1. Estimating patient-specific elasticity distributions

A key step in developing biomechanical breast models for robotic breast immobilization is to develop a well-validated model elasticity reconstruction. The elastic values assigned to the breast tissue for the reported simulation in this work were taken from literature, and manually adjusted by qualitative observation. However, a methodology for patient-specific elasticity estimations has been developed by employing an inverse analysis to prone-supine CT imaging pairs[34]. This work applied a modified Gauss-Newton methodology [35, 36] to optimize a heterogeneous elastic distribution within a breast. The elastic distribution was initialized using the intensity information from the CT to choose an estimated starting point. The optimization scheme minimized the displacement error when applying gravity to one of a prone-supine CT imaging pair, and allowing the model to deform to match the other posture.

A systematic validation of the elasticity reconstruction methodology was accomplished by utilizing the biomechanical simulation to represent a breast in the prone position with a spherical tumor located within the tissue. During the validation procedure, a ground-truth biomechanical model was developed with the spherical tumors being assigned with elasticity values from the literature to represent ductal carcinoma's in-situ, invasive ductal carcinomas (IDC), and fibro-adenomas and positioned with different sizes throughout the breast tissue. The Euclidean distance between \bar{x}_a^n and \bar{x}_a^{n+1} for each mass element was taken to be the ground-truth displacement for that mass element, and then the biomechanical model was reset with an initial guess elastic distribution. The iterative binary search optimization scheme was utilized until convergence occurred.

This elasticity estimation methodology employed the linear elastic material model version of the biomechanical breast model for the forward deformation portion of their optimization scheme. Future work will aim to incorporate the hyper-elastic material model into this optimization to utilize patient-specific elasticity distributions. This should theoretically improve the accuracy of the breast tissue response when manipulated by a virtual immobilization device.

4.2. Moving toward a multi-GPU (mGPU) implementation

Simplifications were applied to the breast model to maintain interactive frame rates for the increased computational complexity of the hyper-elastic material model. These included volumetric simulations of the only the breast anatomy, while replacing the patient torso with a wireframe sphere to model anchoring of the breast to the chest wall. The linear elastic material model was already limited in size by memory capacity of a single GPU, and in speed by the number of processors. Expanding the model to utilize the computational power of a mGPU framework hurdles the previous limitations of the linear material model, and should allow interactive response when simulating a full anatomical model generated from clinical patient data. To our knowledge, this would be the first work to demonstrate a mGPU framework for deforming a high-resolution, patient-specific, volumetric biomechanical model employing hyper-elastic tissue response at interactive speeds.

Moving toward a mGPU implementation, the model will be divided into a system of particle systems: each contoured structure will be a self-contained independent particle system. For the breast model, there was only a single structure of interest, so the others were removed to simplify the simulation and optimize performance to run on a single GPU. For future work, the workload will be distributed with one GPU to calculate the external impulses and structure-structure collisions, while the internal hyper-elastic tissue responses of the individual structures are farmed out to other GPUs as needed. By compartmentalizing the model as a system of smaller particle systems, solving for the internal corrective forces and applied constraints will become smaller independent computations. Additionally, the bony anatomy is considered static, and no elastic connections will be established within them, reducing memory requirements. From this intelligent distribution of the computational effort, we intend to remove the simplifications made to the presented breast model, until we have a fully-functional, interactive, patient-specific model generated from clinical patient imaging. With each structure as an independent system with a triangulated surface, interactions between structures will also need to consider system level, rigid body kinematics such as center of mass position, momentum, and orientation, with additional limitations and constraints to describe unique structure interactions.

4.3. Conclusion

In this paper, we presented a biomechanical breast model for designing and developing a novel soft robotics breast immobilization device. The breast model was developed from patient-specific CT imaging obtained during the treatment planning stage. The breast elasticity can be estimated in a patient-specific manner using an additional CT imaging in the prone posture. An iterative methodology to estimate elasticity by matching the observed deformation between supine and prone imaging has shown good initial results, achieving accuracy of 98% within 1 mm for simulated breast deformations under gravity.

These models can aid in the development of a robotic immobilization device to lift and separate the breast tissue away from the chest wall during external beam radiotherapy treatments to spare exposure of normal tissues. Using the model framework, a virtual robotic system could be tested on an arbitrary number of actual patient data sets to refine its physical design and functional abilities before prototype construction, saving both time and money in research and development. Proposed robotic designs could be loaded into the simulation through volumetric imaging data, or surface definition such as point-cloud vertex lists. The simple soft robotic system presented above for illustration consisted of a stack of tori, the size of which could be controlled by the user. It would be feasible to allow the user to alter the device construction during simulation. Additionally, for future clinical incorporation of the proposed robotic system, patient-specific models will allow planning for positioning, orientation, and other adjustments of the immobilization device prior to patient treatment.

To conclude, we believe patient-specific biomechanical models can be a valuable resource for the development, validation, and implementation of robotic interventional technology in the clinic. A platform providing realistic, interactive tissue response simulations can accelerate development by facilitating faster design iterations without the requirement for a physical manufacturing. We also expect that further development will expand the possible applications for such models.

REFERENCES

- [1] Kirby, A. M., Evans, P. M., Helyer, S. J., Donovan, E. M., Convery, H. M., and Yarnold, J. R., "A randomised trial of supine versus prone breast radiotherapy (SuPr study): comparing set-up errors and respiratory motion," *Radiother Oncol* 100(2), 221-6 (2011).
- [2] Padilla, L., Kang, H., Washington, M., Hasan, Y., Chmura, S. J., and Al-Hallaq, H., "Assessment of interfractional variation of the breast surface following conventional patient positioning for whole-breast radiotherapy," *J Appl Clin Med Phys* 15(5), 4921 (2014).
- [3] Fatunase, T., Wang, Z., Yoo, S., Hubbs, J. L., Prosnitz, R. G., Yin, F. F., and Marks, L. B., "Assessment of the residual error in soft tissue setup in patients undergoing partial breast irradiation: results of a prospective study using cone-beam computed tomography," *Int J Radiat Oncol Biol Phys* 70(4), 1025-34 (2008).
- [4] Jain, P., Marchant, T., Green, M., Watkins, G., Davies, J., McCarthy, C., Loncaster, J., Stewart, A., Magee, B., Moore, C., and Price, P., "Inter-fraction motion and dosimetric consequences during breast intensity-modulated radiotherapy (IMRT)," *Radiother Oncol* 90(1), 93-8 (2009).
- [5] Michalski, A., Atyeo, J., Cox, J., and Rinks, M., "Inter- and intra-fraction motion during radiation therapy to the whole breast in the supine position: a systematic review," *J Med Imaging Radiat Oncol* 56(5), 499-509 (2012).
- [6] Sifakis, E., Neverov, I., and Fedkiw, R., "Automatic determination of facial muscle activations from sparse motion capture marker data," *ACM Transactions on Graphics* 24(3), 417-425 (2005).
- [7] Albrecht, I., Haber, J., and Seidel, H., "Construction and animation of anatomically based human hand models," *ACM Siggraph*, 98-109 (2003).
- [8] Tsang, W., Singh, K., and Fiume, E., "Helping hand: An anatomically accurate inverse dynamics solution for unconstrained hand motion.," *ACM Siggraph*, 319-328 (2005).
- [9] Santhanam, A., Willoughby, T., Shah, A., Meeks, S. L., Rolland, J. P., and Kupelian, P., "Real-time Simulation of 4D lung tumor radiotherapy using a breathing model," *Lecture Notes on Computer Science* 11, 710-717 (2008).
- [10] Komura, T., Shinagawa, Y., and Kunii, T. L., "Creating and retargeting motion by the musculoskeletal human body model," *The visual computer* 16(5), 254-270 (2000).

- [11] Neylon, J., Qi, X., Sheng, K., Staton, R., Pukala, J., Manon, R., Low, D. A., Kupelian, P., and Santhanam, A., "A GPU based high-resolution multilevel biomechanical head and neck model for validating deformable image registration," *Med Phys* 42(1), 232-43 (2015).
- [12] Fung, Y. C., "Elasticity of soft tissues in simple elongation," *Am J Physiol* 213(6), 1532-44 (1967).
- [13] Fung, Y. C., [Biomechanics: Mechanical Properties of Living Tissues], New York: Springer, 568, (1993).
- [14] Picinbono, G., Delingette, H., and Ayache, N., "Non-linear anisotropic elasticity for real-time surgery simulation," *Graphical Models* 65, 305-321 (2003).
- [15] Doyley, M. M. and Parker, K. J., "Elastography: general principles and clinical applications," *Ultrasound Clin* 9(1), 1-11 (2014).
- [16] Doyley, M. M., Srinivasan, S., Pendergrass, S. A., Wu, Z., and Ophir, J., "Comparative evaluation of strain-based and model-based modulus elastography," *Ultrasound Med Biol* 31(6), 787-802 (2005).
- [17] Zhi, H., Xiao, X. Y., Yang, H. Y., Wen, Y. L., Ou, B., Luo, B. M., and Liang, B. L., "Semi-quantitating stiffness of breast solid lesions in ultrasonic elastography," *Acad Radiol* 15(11), 1347-53 (2008).
- [18] Bhatti, S. N. and Sridhar-Keralapura, M., "A novel breast software phantom for biomechanical modeling of elastography," *Med Phys* 39(4), 1748-68 (2012).
- [19] Rychlewski, J., "On Hooke's Law," *Journal of Applied Mathematics and Mechanics* 48(3), 303-314 (1984).
- [20] Ogden, R. W., "Large Deformation Isotropic Elasticity: On the Correlation of Theory and Experiment for Compressible Rubberlike Solids," *Proceedings of the Royal Society of London. Series A: Mathematical and Physical Sciences* 326(1567), 565-584 (1972).
- [21] Korhonen, R. K. and Saarakkala, S., "Biomechanics and Modeling of Skeletal Soft Tissues," in [Theoretical Biomechanics], V. Klika, Editor, InTech (2011).
- [22] Mooney, M., "A theory of large elastic deformation," *Journal of Applied Physics* 11(9), 582-592 (1940).
- [23] Rivlin, R. S., "Large elastic deformations of isotropic materials. IV. Further developments of the general theory," *Philosophical Transactions of the Royal Society of London. Series A: Mathematical and Physical Sciences* 241(835), 379-397 (1948).
- [24] Natali, A., Carniel, E., Pavan, P., Dario, P., and Izzo, I. "Hyperelastic models for the analysis of soft tissue mechanics: definition of constitutive parameters," in *Biomedical Robotics and Biomechatronics*, Pisa: IEEE (2006).
- [25] Hoogstraten, P. A. A. v., Slaats, P. M. A., and Baaijens, F. P. T., "A Eulerian approach to the finite element modelling of neo-Hookean rubber material," *Applied Scientific Research* 48, 193-210 (1990).
- [26] Hibbit, Karlsson, and Sorensen, [ABAQUS theory manual], Pawtucket, RI, (1998).
- [27] Ascher, U. and Petzold, L., [Computer Methods for Ordinary Differential Equations and Differential-Algebraic Equations], Philadelphia, PA: Society for Industrial and Applied Mathematics, (1998).
- [28] Suli, E. and Mayers, D., [An Introduction to Numerical Analysis], Cambridge, UK: Cambridge University Press, (2003).
- [29] Lorensen, W. E. and Cline, H. E., "Marching Cubes: A High Resolution 3D Surface Construction Algorithm," *ACM Computer Graphics* 21(4), 163-169 (1987).
- [30] Hilton, A. and Illingworth, H., "Marching Triangles: Range Image Fusion for Complex Object Modeling," *Image Processing 1*, 381-384 (1996).
- [31] Bernardini, F., Mittleman, J., Rushmeier, H., Silva, C., and Taubin, G., "The Ball-Pivoting Algorithm for Surface Reconstruction," *IEEE Transactions on Visualization and Computer Graphics* 5(4), 349-359 (1999).
- [32] Kazhdan, M., Bolitho, M., and Hoppe, H., "Poisson Surface Reconstruction," *Eurographics Symposium on Geometry Processing* (2006).
- [33] Hong, M., Jung, S., Choi, M.-H., and Welch, S., "Fast Volume Preservation for a Mass-Spring System," *IEEE Computer Graphics and Applications*, 83-91 (2006).
- [34] Hasse, K., Neylon, J., Sheng, K., and Santhanam, A., "Systematic feasibility analysis of a quantitative elasticity estimation for breast anatomy using supine/prone patient postures," *Medical Physics* 43(3) (2016).
- [35] Gill, P. E., Murray, W., and Wright, M. H., [Practical optimization]: Academic Press, (1981).
- [36] Kallel, F. and Bertrand, M., "Tissue elasticity reconstruction using linear perturbation method," *IEEE Transactions on Medical Imaging* 15(3), 299-313 (1996).